Research Square

Preprints are preliminary reports that have not undergone peer review.
They should not be considered conclusive, used to inform clinical practice,
or referenced by the media as validated information.

Deformation Mechanisms of Three-Dimensional Angle-Interlock Preforms

Zhenyu Wang
TianGong University
Yifan Zhang
zhangyifan@tiangong.edu.cn
TianGong University
Jiahui Wei
TianGong University
Qiwei Guo
Tianjin Normal University
Daijun Zhang
AECC Beijing Institute of Aeronautical Materials
Chao Li
Nanjing Fiberglass Research & Design Institute
Junjie Hao
Shanxi Gangke Carbon Materials Co., Ltd
Pengfei Jiang
Beijing Composite Materials Co., Ltd
Tianqi Wang
TianGong University
Li Chen
TianGong University

Research Article

Keywords: Three-dimensional angle-interlock preform, Anisotropic hyperelastic constitutive model, Finite element analysis, Nonlinear mechanical behavior

Posted Date: August 19th, 2026

DOI: https://doi.org/10.21203/rs.3.rs-10382754/v1

License: This work is licensed under a Creative Commons Attribution 4.0 International License.
Read Full License

Additional Declarations: No competing interests reported.

Deformation Mechanisms of Three-Dimensional Angle-Interlock Preforms

Zhenyu Wang [a,b], Yifan Zhang [a,c*], Jiahui Wei [a,c], Qiwei Guo [d], Daijun Zhang [e], Chao Li [f], Junjie Hao [g], Pengfei Jiang [h], Tianqi Wang [a,b**], Li Chen [a,c]

a. Ministry of Education Key Laboratory of Advanced Textile Composite Materials, TianGong University, Tianjin 300387, China

b. School of mechanical engineering, TianGong University, Tianjin 300387, China

c. School of textile science and engineering, TianGong University, Tianjin 300387, China

d. College of Fine Arts & Design, Tianjin Normal University, Tianjin 300387, China

e. AECC Beijing Institute of Aeronautical Materials, Beijing 100095, China

f. Nanjing Fiberglass Research & Design Institute, Nanjing 211101, China

g. Shanxi Gangke Carbon Materials Co., Ltd., Taiyuan 030100, China

h. Beijing Composite Materials Co., Ltd., Beijing 100192, China

Abstract: To characterize the nonlinear, anisotropic, and large-deformation behavior of three-dimensional angle-interlock preforms during forming over complex surfaces, a multi-mode decoupled hyperelastic constitutive model is established. Based on structural tensors and physical invariants associated with different deformation modes, strain energy density functions are formulated for warp/weft tension, thickness compression, in-plane shear, and out-of-plane shear, and the corresponding material parameters are identified through mechanical characterization tests. The model is implemented in ABAQUS via a VUMAT user material subroutine, and its predictive capability for complex-surface forming is validated by hemispherical forming experiments. The results show that the established model can reasonably predict the load–displacement response, the in-plane shear angle distribution on the convex side, and the boundary draw-in behavior during forming. The relative errors in the peak load and the peak shear angle along the 45° path on the convex side are 15.2% and 6.3%, respectively. During forming, in-plane shear is the dominant deformation mode, with a maximum shear angle of 37.4°, mainly located in the curvature transition region between the hemispherical punch-contact region and the flange region on the concave side. The sectional out-of-plane shear angle remains relatively low overall, with elevated values mainly concentrated in the bending transition zones of the sections. Different initial yarn orientations primarily alter the spatial distribution of high-shear regions and the boundary contour evolution, while exerting limited influence on the maximum shear angle. These results provide a reference for the forming simulation and process optimization of three-dimensional woven preforms over complex surfaces.

Keywords: Three-dimensional angle-interlock preform; Anisotropic hyperelastic constitutive

* Correspondence to: School of Textile Science and Engineering, Tiangong University, No. 399 West Binshui Road, Xiqing District, Tianjin, 300387, China.

E-mail address: zhangyifan@tiangong.edu.cn (Y. Zhang)

** Correspondence to: School of Mechanical Engineering, Tiangong University, No. 399 West Binshui Road, Xiqing District, Tianjin, 300387, China.

E-mail address: wtq0622@163.com (T. Wang)

model; Finite element analysis; Nonlinear mechanical behavior

1 Introduction

Angle-interlock preforms are representative three-dimensional woven reinforcements with strong potential for aerospace, marine, and defense applications owing to their spatially interlocked yarn architecture, excellent through-thickness reinforcement, and high specific strength [1–7]. Compared with conventional two-dimensional laminated structures, angle-interlock preforms exhibit superior resistance to delamination, improved structural integrity, and better formability, as well as enhanced through-thickness stability during subsequent resin impregnation and curing. However, during forming over complex surfaces, a planar preform must conform to a three-dimensional geometry, accompanied by significant changes in yarn trajectories, interlacing angles, and local deformation states. As a result, the preform exhibits pronounced nonlinear, anisotropic, and coupled deformation behavior.

To characterize the complex deformation behavior of textile reinforcements, extensive numerical modeling approaches have been developed at different scales [8–13]. In simulations of composite preform forming, early kinematic models, such as the Chebyshev net method [14], offer high computational efficiency but do not explicitly account for the intrinsic mechanical response of textile reinforcements, which limits their ability to predict forming defects under complex processing conditions. To elucidate mesoscopic deformation mechanisms, discrete models have been proposed in which yarns are represented by beam or spring elements [15–18]. Although these models can effectively capture yarn–yarn interactions, their application to large-scale industrial components is often limited by high computational cost. By contrast, macroscopic constitutive models based on continuum mechanics regard the preform as an equivalent continuum and describe its overall mechanical response at the component scale. Owing to their favorable balance between predictive accuracy and computational efficiency, these models have become an important tool for fabric forming simulations.

Within the framework of continuum mechanics, various constitutive models have been proposed to describe the macroscopic mechanical behavior of textile reinforcements. Among them, non-orthogonal constitutive models track fiber orientations by introducing a non-orthogonal coordinate system that evolves with material deformation, and are capable of describing large-angle shear deformation during forming [19–21]. Hypoelastic models are formulated in a stress-rate form and are convenient for numerical implementation; however, their dependence on the selected objective stress rate may lead to non-physical responses and numerical stability issues [22]. Hyperelastic constitutive models are constructed based on strain energy density functions and satisfy the requirement of thermodynamic consistency. They are therefore suitable for describing the mechanical response of textile reinforcements under large-deformation and anisotropic conditions, and have received considerable attention in fabric forming simulations in recent years [23–29]. The characteristic formulations and key features of these commonly used macroscopic modeling approaches are schematically summarized in Fig. 1.

In terms of the construction of strain energy functions, existing studies have generally focused on decomposing the dominant deformation modes of textile reinforcements and developing hyperelastic constitutive models in different forms. Peng et al. [25] decomposed the total strain energy density function of two-dimensional woven fabrics into tensile and shear strain energy components at the macroscopic scale, and determined the corresponding energy functions based on

uniaxial tensile and picture-frame shear tests. Following this framework, Yin et al. [26] applied the model to the draping simulation of two-dimensional woven fabrics over double-curvature molds, achieving effective prediction of the fabric forming process. For more complex fabric architectures, Charmetant et al. [27] developed a hyperelastic constitutive framework for large-deformation analyses of three-dimensional interlock composite preforms, providing an important theoretical basis for the forming simulation of three-dimensional woven preforms.

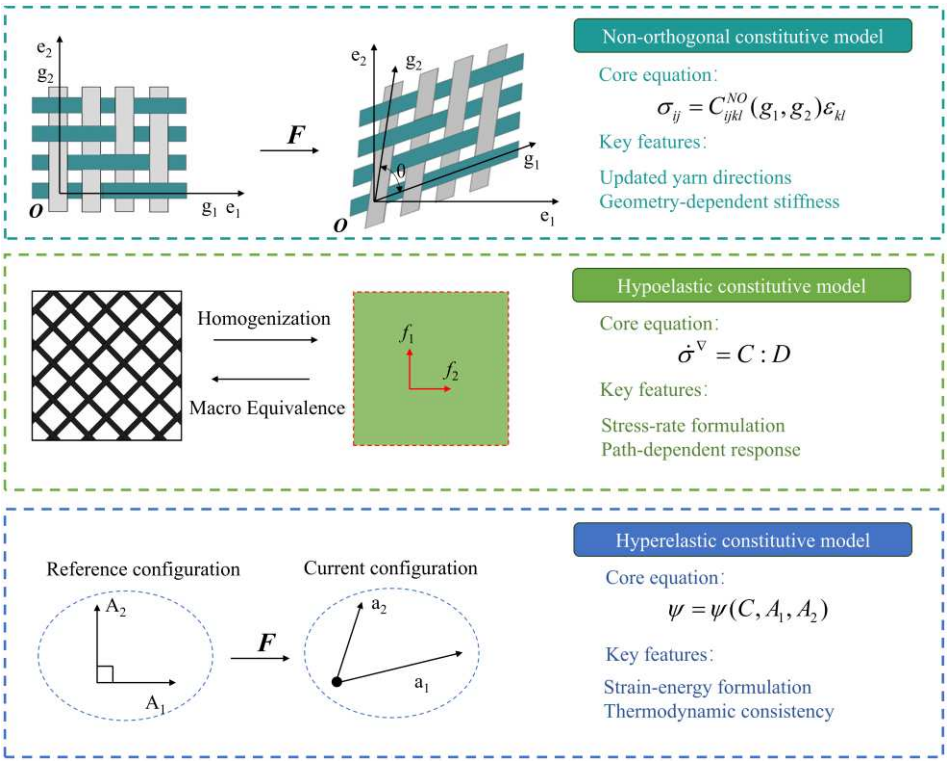


Fig. 1 Schematic illustration of macroscopic constitutive models: non-orthogonal elastic model, hypoelastic model, and hyperelastic model

Based on continuum mechanics, a multi-mode decoupled anisotropic hyperelastic constitutive framework is established in this study to simulate the forming behavior of a 1/3 twill three-dimensional angle-interlock preform. The material parameters are identified through mechanical characterization tests, including tension, compression, and shear tests, and the constitutive model is implemented in ABAQUS via a user-defined VUMAT subroutine. The predictive accuracy of the model is validated against hemispherical forming experiments in terms of the load–displacement response, in-plane shear angle distribution, and boundary draw-in after forming. The local three-dimensional out-of-plane shear deformation mechanism is then further analyzed. Finally, the effects of initial yarn orientation on the overall shear field and boundary contour evolution are investigated.

2 Hyperelastic Constitutive Framework

2.1 Fundamental Relations of Finite-Deformation Hyperelasticity

Three-dimensional woven preforms typically undergo large deformation and exhibit anisotropic and nonlinear mechanical responses during forming. To describe such behavior, a macroscopic constitutive framework based on hyperelastic theory is established in this study, in which the mechanical response of the material is represented by a strain energy density function [23–25].

In finite-deformation theory, the motion of a material point from the reference configuration to the current configuration is described by the deformation gradient tensor $\boldsymbol{F}$. To satisfy the requirement of material objectivity, the right Cauchy–Green deformation tensor $\boldsymbol{C}$ is commonly adopted as the deformation measure, which is defined as:

$$\boldsymbol{C} = \boldsymbol{F}^{\mathrm{T}}\boldsymbol{F} \tag{1}$$

Based on this deformation measure, the strain energy density function ψ can be expressed as a scalar function of the right Cauchy–Green deformation tensor $\boldsymbol{C}$:

$$\psi = \psi(\mathbf{C}) \tag{2}$$

According to hyperelastic theory, the second Piola–Kirchhoff stress tensor $\boldsymbol{S}$, which is work-conjugate to the right Cauchy–Green deformation tensor $\boldsymbol{C}$, is obtained by differentiating the strain energy density function with respect to $\boldsymbol{C}$:

$$\mathbf{S} = 2\frac{\partial \psi}{\partial \mathbf{C}} \tag{3}$$

To express the stress response in the current configuration, the Cauchy stress tensor $\boldsymbol{\sigma}$ can be calculated through the push-forward operation using the deformation gradient tensor $\boldsymbol{F}$, together with the Jacobian determinant $J = \det(\boldsymbol{F})$, which characterizes the volume change:

$$\boldsymbol{\sigma} = \frac{1}{J}\boldsymbol{F}\boldsymbol{S}\boldsymbol{F}^{\mathrm{T}} \tag{4}$$

2.2 Definition of Structural Tensors and Mixed Invariants

To describe the anisotropic behavior of three-dimensional woven preforms, a local orthogonal material coordinate system is defined in the reference configuration. Three mutually orthogonal unit vectors, $\boldsymbol{a}_1$, $\boldsymbol{a}_2$ and $\boldsymbol{a}_3$ are introduced to represent the initial warp, weft, and thickness directions, respectively [27–29]. Based on these material direction vectors, the structural tensors associated with the principal material directions are defined as:

$$\boldsymbol{A}_i = \boldsymbol{a}_i \otimes \boldsymbol{a}_i, i = 1,2,3 \tag{5}$$

Furthermore, a set of mixed invariants can be constructed from the right Cauchy–Green deformation tensor $\boldsymbol{C}$ and the material direction vectors to characterize the deformation along the principal material directions and the directional coupling between them:

$$\begin{aligned} &I_4 = \boldsymbol{a}_1 \cdot (\boldsymbol{C}\boldsymbol{a}_1) \quad I_6 = \boldsymbol{a}_2 \cdot (\boldsymbol{C}\boldsymbol{a}_2) \quad I_8 = \boldsymbol{a}_3 \cdot (\boldsymbol{C}\boldsymbol{a}_3) \\ &I_{46} = \boldsymbol{a}_1 \cdot (\boldsymbol{C}\boldsymbol{a}_2) \quad I_{48} = \boldsymbol{a}_1 \cdot (\boldsymbol{C}\boldsymbol{a}_3) \quad I_{68} = \boldsymbol{a}_2 \cdot (\boldsymbol{C}\boldsymbol{a}_3) \end{aligned} \tag{6}$$

Here, I_4, I_6 and I_8 describe the deformation along the warp, weft, and thickness directions, respectively, whereas I_{46}, I_{48} and I_{68} characterize the coupling deformation between different material directions. These mixed invariants provide the basis for constructing physical invariants associated with tension, thickness compression, in-plane shear, and out-of-plane shear.

2.3 Multi-Mode Decoupled Strain Energy Function and Stress Formulation

The macroscopic deformation of three-dimensional angle-interlock preforms can be decomposed into four fundamental modes: warp/weft tension, through-thickness compression, in-plane shear, and out-of-plane shear [25,27–29]. Warp/weft tension represents the axial load-bearing response of yarns along the principal material directions, while through-thickness compression characterizes the compaction of the preform in the thickness direction. In-plane shear describes the relative rotation between warp and weft yarns at the interlacing points, whereas out-

of-plane shear reflects the through-thickness deflection of the warp and weft yarn systems.

Based on this decoupling strategy, the total strain energy density function can be expressed as the sum of the energy contributions associated with the fundamental deformation modes. For a three-dimensional woven preform with three orthogonal material principal directions, the mixed invariants constructed from $\boldsymbol{C}$ and the material direction vectors are transformed into physical invariants corresponding to specific deformation modes. The total strain energy density function can then be written as a scalar function of these physical invariants:

$$\psi(\boldsymbol{C}) = \psi_{\text{elong}}(I_{\text{elong1}}) + \psi_{\text{elong}}(I_{\text{elong2}}) + \psi_{\text{comp}}^{\text{thick}}(I_{\text{comp}}) + \psi_{\text{shear}}^{\text{in-plane}}(I_{\text{cp}}) + \psi_{\text{shear}}^{\text{out-plane}}(I_{\text{ct1}}) + \psi_{\text{shear}}^{\text{out-plane}}(I_{\text{ct2}}) \tag{7}$$

where ψ_{elong}, ψ_{comp}, $\psi_{\text{shear}}^{\text{in-plane}}$, and $\psi_{\text{shear}}^{\text{out-plane}}$ denote the strain energy density components associated with tension, thickness compression, in-plane shear, and out-of-plane shear, respectively. The corresponding physical invariants are defined as:

$$\begin{aligned}
&I_{\text{elong1}} = \ln\sqrt{I_4} && I_{\text{elong2}} = \ln\sqrt{I_6} \\
&I_{\text{comp}} = \ln\left(\sqrt{\frac{\det(\boldsymbol{C})}{I_4 I_6}}\right) && I_{\text{cp}} = \frac{I_{46}}{\sqrt{I_4 I_6}} = \sin(\gamma) \\
&I_{\text{ct1}} = \frac{I_{48}}{\sqrt{I_4 I_8}} = \sin(\gamma_{4,8}) && I_{\text{ct2}} = \frac{I_{68}}{\sqrt{I_6 I_8}} = \sin(\gamma_{6,8})
\end{aligned} \tag{8}$$

Here, I_{elong1} and I_{elong2} are the logarithmic elongation variables in the warp and weft directions, respectively; I_{comp} is the compaction-related invariant in the thickness direction; I_{cp} represents the sine of the in-plane shear angle; I_{ct1} and I_{ct2} are the invariants associated with out-of-plane shear; and $\det(\boldsymbol{C})$ is the determinant of the right Cauchy–Green deformation tensor $\boldsymbol{C}$.

In finite element calculations, the stress response in the current configuration is usually represented by the Cauchy stress tensor $\boldsymbol{\sigma}$. According to Eq. (4), $\boldsymbol{\sigma}$ can be obtained from the second Piola–Kirchhoff stress tensor $\boldsymbol{S}$. Based on Eqs. (3), (7), and (8), $\boldsymbol{S}$ can be expanded using the chain rule as

$$\boldsymbol{S} = 2\left(\sum_{i=1}^{2} \frac{\partial \psi_{\text{elong}i}}{\partial I_{\text{elong}i}} \frac{\partial I_{\text{elong}i}}{\partial \boldsymbol{C}} + \frac{\partial \psi_{\text{comp}}^{\text{thick}}}{\partial I_{\text{comp}}} \frac{\partial I_{\text{comp}}}{\partial \boldsymbol{C}} + \frac{\partial \psi_{\text{shear}}^{\text{in-plane}}}{\partial I_{\text{cp}}} \frac{\partial I_{\text{cp}}}{\partial \boldsymbol{C}} + \sum_{i=1}^{2} \frac{\partial \psi_{\text{shear}}^{\text{out-plane}}}{\partial I_{\text{ct}i}} \frac{\partial I_{\text{ct}i}}{\partial \boldsymbol{C}}\right) \tag{9}$$

In Eq. (9), the derivatives of the energy functions are obtained from the specific forms of the strain energy density functions for the corresponding deformation modes, whereas the derivatives of the physical invariants with respect to the right Cauchy–Green deformation tensor $\boldsymbol{C}$ can be derived from their definitions.

3 Mechanical Characterization and Constitutive Parameter Identification

The investigated material was a three-dimensional angle-interlock preform manufactured from TG800HX-12K carbon fiber yarns. The constituent carbon fiber yarns were supplied by Shanxi Gangke Carbon Materials Co., Ltd., and the preform was fabricated by the Institute of Composite Materials, Tiangong University. The basic properties of the TG800HX-12K carbon fiber yarns are summarized in Table 1.

Table 1 Properties of TG800HX-12K carbon fiber yarns

Fiber type	Tensile modulus (GPa)	Linear density ($g \cdot km^{-1}$)	Bulk density ($g \cdot cm^{-3}$)	Elongation ratio (%)
TG800HX-12K	294	445	1.8	1.9

The preform thickness, yarn specifications, yarn densities, and corresponding experimental items are listed in Table 2.

Table 2 Structural parameters of the three-dimensional angle-interlock preform

Fabric thickness (mm)	Yarn type	Yarn specification	Yarn density (ends or picks·cm^{-1})	Experimental items
4.5	Warp yarn	TG800HX-12K×2	5±0.2	Uniaxial tension, transverse compression, and in-plane shear
	Weft yarn	TG800HX-12K×2	3±0.2	
9.0	Warp yarn	TG800HX-12K×2	5±0.2	Out-of-plane shear
	Weft yarn	TG800HX-12K×2	3±0.2	

Fig. 2 shows a schematic representation of the architecture of the three-dimensional angle-interlock preform. The preform consists of warp and weft yarn systems, in which the warp yarns follow undulated paths along the thickness direction and interlace with adjacent weft yarn layers, forming a continuous through-thickness angle-interlock architecture. Owing to differences in warp/weft yarn densities and spatial interlacing paths, the preform exhibits pronounced anisotropic mechanical responses under tensile, compressive, and shear loading. Therefore, its mechanical behavior was characterized through uniaxial tension, transverse compression, in-plane shear, and out-of-plane shear tests in this section. The corresponding loading configurations are shown in Fig. 3. Three valid datasets were obtained for each test and then averaged. Based on the experimental curves, the parameters of the strain energy density functions in the hyperelastic constitutive model were identified.

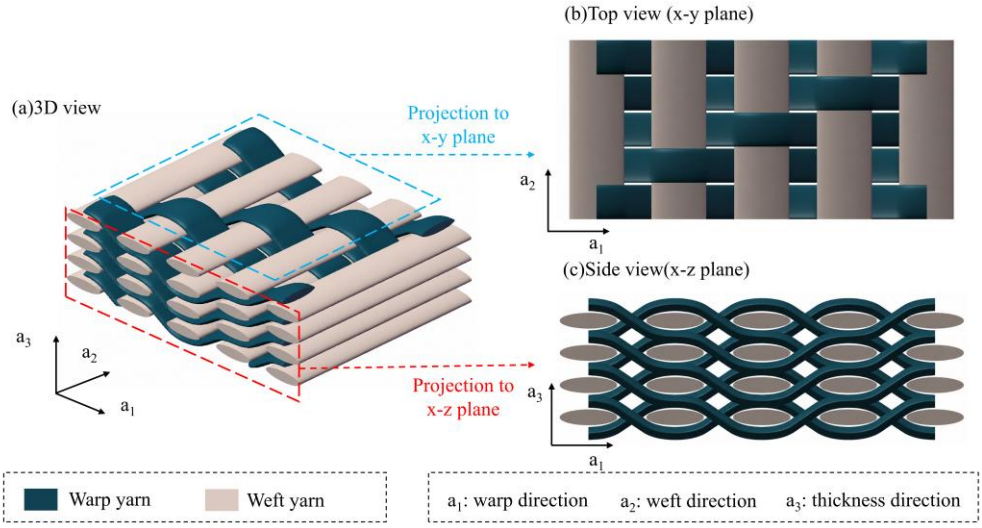


Fig. 2 Schematic architecture of the three-dimensional angle-interlock preform: (a) three-dimensional view; (b) top view in the x–y plane; (c) side view in the x–z plane

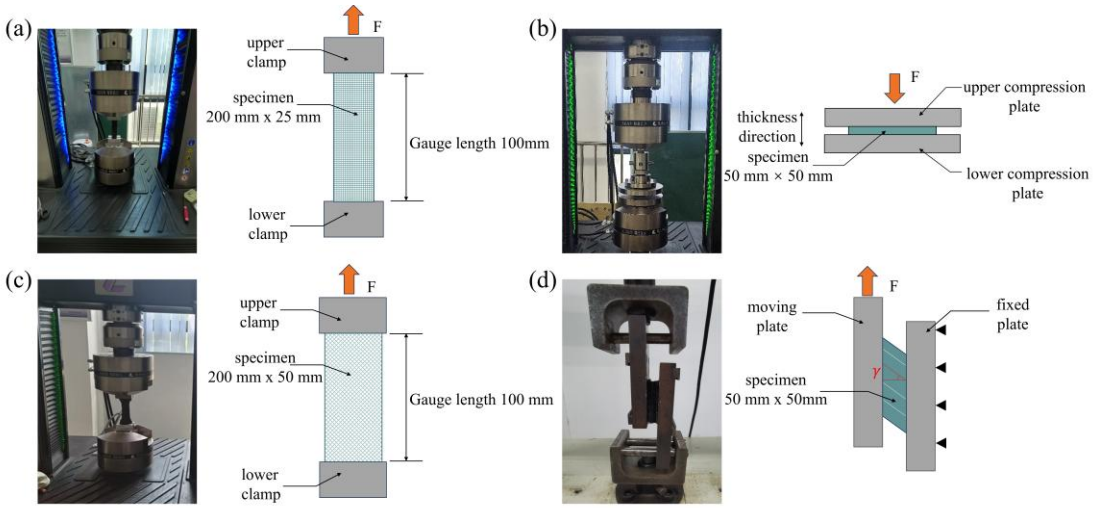


Fig. 3 Experimental setups and loading configurations for the basic mechanical tests of the three-dimensional angle-interlock preform: (a) uniaxial tension; (b) transverse compression; (c) bias-extension; (d) out-of-plane shear

3.1 Uniaxial Tension Test

Uniaxial tension tests of the three-dimensional angle-interlock preform were conducted using a universal testing machine. Specimens were cut along the warp and weft yarn directions, with dimensions of 200 mm × 25 mm. The gauge region was 100 mm × 25 mm. To prevent slippage during loading, the clamping regions at both ends of each specimen were impregnated with resin and cured, with a cured length of 50 mm at each end. The loading rate was set to 2 mm/min.

Fig. 5(a) and (b) show the load–displacement curves of the three-dimensional angle-interlock preform under warp- and weft-direction uniaxial tension, respectively. Pronounced nonlinear tensile responses are observed in both directions. In the initial loading stage, the load increases slowly with displacement, indicating a low-stiffness response. This is mainly attributed to the gradual straightening of the initially crimped yarns and local relative sliding between yarns. As the tensile displacement further increases, the yarns are progressively straightened, and the tensile load is mainly borne by the carbon fiber yarn bundles. Consequently, the load increases continuously with displacement, exhibiting nonlinear stiffening.

3.2 Transverse Compression Test

Transverse compression behavior of the three-dimensional angle-interlock preform was characterized using a universal testing machine. Square specimens measuring 50 mm × 50 mm were subjected to thickness compression with a rigid circular platen of 200 mm in diameter. A relatively large platen was selected to minimize the effect of local contact irregularities and ensure a more uniform loading condition. Tests were conducted at a displacement rate of 1 mm/min, with the compression displacement limited to 2 mm.

Fig. 5(c) shows the load–displacement curve of the three-dimensional angle-interlock preform under transverse compression, which exhibits a pronounced nonlinear increase. In the initial compression stage, the platen comes into contact with the preform surface, and the load increases slowly with displacement. As the dry preform consists of spatially interlaced warp and weft yarns, numerous inter-yarn voids exist between yarn bundles and in the interlacing regions. The deformation in this stage is mainly governed by the closure of these structural voids, slight relative movement between yarns, and weak contact friction [30–33]. Meanwhile, the external load has not yet induced significant transverse compaction of the fiber bundles themselves; therefore, the

material exhibits relatively low initial stiffness.

With increasing compression displacement, the inter-yarn voids are gradually closed. The dominant deformation mechanism shifts from structural compaction between yarn bundles to transverse rearrangement and mutual compaction of fibers within the yarn bundles. The inter-fiber voids are progressively eliminated, and the fiber volume fraction continuously increases, leading to a pronounced nonlinear increase in compressive stiffness.

3.3 In-Plane Shear Test

The in-plane shear behavior of the three-dimensional angle-interlock preform was characterized using bias-extension tests [34–39], which were conducted on a universal testing machine. Specimens measuring 200 mm × 50 mm were prepared such that the warp and weft yarns were oriented at ±45° relative to the loading direction. The gauge region was 100 mm × 50 mm, and the clamping length at each end was 50 mm. The loading rate was 3 mm/min.

The bias-extension test provides the axial load–displacement response of the specimen rather than the in-plane shear response directly. Therefore, before analyzing the shear behavior, the original load–displacement data were normalized and converted into a shear force–shear angle relationship associated with in-plane shear deformation. In this study, the kinematic model shown in Fig. 4 was adopted, in which the deformation region of the bias-extension specimen was divided into an undeformed end region (region A), a half-shear region (region B), and a pure shear region (region C). Region C is located away from the clamping ends and is less affected by boundary constraints, thereby providing a more representative shear deformation state. Therefore, the shear angle in region C was selected to characterize the in-plane shear deformation. Based on the principle of virtual work, the experimental data were normalized to obtain the shear force–shear angle relationship [35,36,40]. According to the geometric relationship shown in Fig. 4, the relationship between the shear angle in region C and the tensile displacement can be expressed as follows:

$$\gamma = 90° - 2\theta = 90° - 2\cos^{-1}\frac{L_0 + \delta}{\sqrt{2}L_0} \tag{10}$$

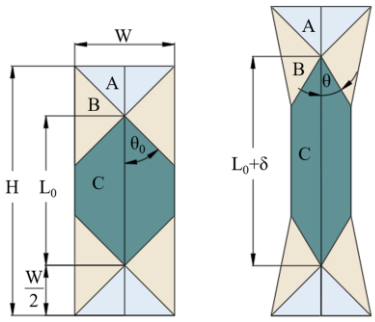


Fig. 4 Division of deformation regions in the bias-extension test and the kinematic theoretical model

Based on the principle of virtual work, the external work done by the axial tensile force (F) is related to the shear strain energy stored in the deforming regions of the specimen. Considering the initial gauge length (H), specimen width (W), and the areas of the different deformation regions, the normalized shear force in the pure shear region can be obtained by substituting the shear angle calculated from Eq. (10):

$$F_{sh}(\gamma) = \frac{1}{(2H - 3W)\cos\gamma}\left[\left(\frac{H}{W} - 1\right)F\left(\cos\frac{\gamma}{2} - \sin\frac{\gamma}{2}\right) - WF_{sh}\left(\frac{\gamma}{2}\right)\cos\frac{\gamma}{2}\right] \tag{11}$$

where γ is the shear angle in the pure shear region C, W is the specimen width, H is the specimen gauge length, δ is the crosshead displacement, F is the tensile load of the specimen, and F_{sh} is the shear force in the pure shear region C.

After the shear force $F_{sh}(\gamma)$ is obtained from Eq. (11), it is converted into the unit torque C_s in the initial unit-volume region according to the normalization relationship of the bias-extension test:

$$C_s = F_{sh}(\gamma) \cdot \cos(\gamma) \tag{12}$$

The in-plane shear strain energy density function can then be obtained by integrating the unit torque C_s with respect to the shear angle γ and dividing it by the specimen thickness t:

$$\psi(\gamma) = \int_0^{\gamma} \frac{C_s}{t} \mathrm{d}\gamma \tag{13}$$

During the bias-extension test, the central region of the specimen undergoes pronounced transverse contraction. Under tensile loading, the initially orthogonal warp and weft yarns rotate relative to each other, and the yarn angle continuously decreases, resulting in a skewed rhombic deformation pattern, as shown in Fig. 3(c). Compared with the clamped regions at both ends, the pure shear region C is less affected by constraints imposed by the clamps, leading to more representative yarn rotation and more pronounced in-plane shear deformation.

Fig. 5(d) shows the load–displacement curve obtained from the bias-extension test. The curve reflects the staged nonlinear response associated with the in-plane shear deformation of the preform. In the initial stage, the deformation is dominated by relative yarn rotation around the interlacing points, and the shear stiffness remains relatively low. As the displacement increases, the yarn angle further decreases, and transverse contact and compaction between yarns become more pronounced. This restricts relative yarn rotation and leads to a rapid increase in shear resistance [41,42]. With further displacement, the preform exhibits a tendency toward shear locking, accompanied by local yarn wrinkling or nonuniform deformation [43,44], which results in changes in the curve slope and increased data scatter.

3.4 Out-of-Plane Shear Test

Out-of-plane shear tests of the three-dimensional angle-interlock preform were conducted using a Shimadzu material testing machine (AGS-J, 1 kN). Specimens with dimensions of 50 mm × 50 mm and a thickness of 9.0 mm were used, and the corresponding structural parameters are listed in Table 2. The test fixture is shown in Fig. 3(d). During the test, the upper and lower surfaces of the specimen were bonded to the fixed and moving plates respectively, using thin double-sided adhesive tape. Out-of-plane shear deformation was imposed by the relative translation between the two plates. The loading rate was 3 mm/min. The experimental data were normalized and processed based on a variational formulation for the identification of out-of-plane shear parameters.

As shown in Fig. 5(e) and (f), the preform exhibits similar load–displacement responses under out-of-plane shear in the warp and weft directions. The load increases rapidly in the initial loading stage, followed by a gradual decrease in tangent stiffness with increasing displacement until the response approaches a plateau. This behavior is mainly attributed to the geometric constraint and static friction of the warp–weft interlacing network against relative interlayer movement during the initial shear stage. As the displacement increases, local rearrangement and structural relaxation occur within the yarn network, leading to a gradual reduction in the incremental shear resistance.

Although the overall response trends are similar, the shear load in the weft direction is higher than that in the warp direction under the same shear displacement. This difference mainly results from the asymmetric warp/weft yarn densities and the different spatial interlacing paths within the preform. When relative interlayer movement occurs in the weft direction, yarn sliding is more

strongly constrained by the interlacing points because the warp yarn density is higher than the weft yarn density. Consequently, higher internal frictional resistance is generated.

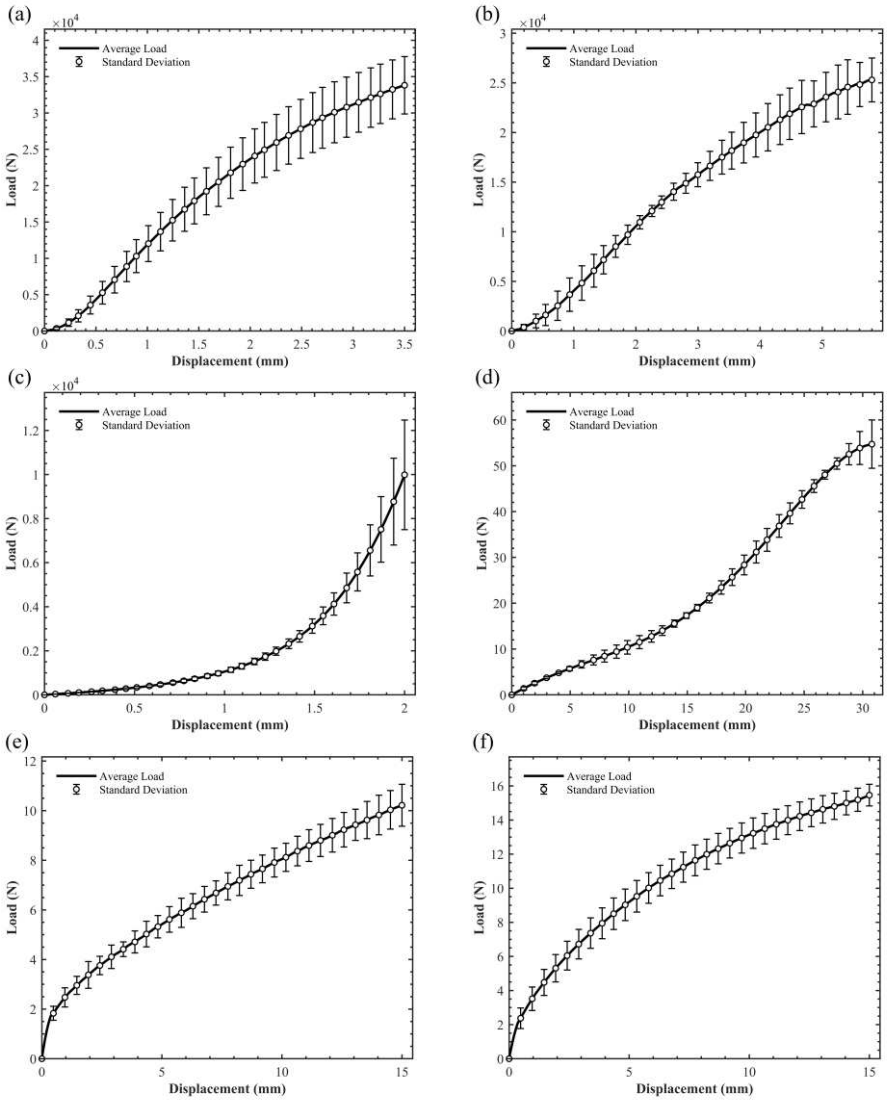


Fig. 5 Load–displacement responses under different fundamental deformation modes: (a) warp-direction tension; (b) weft-direction tension; (c) transverse compression; (d) in-plane shear; (e) warp-direction out-of-plane shear; (f) weft-direction out-of-plane shear

3.5 Identification of Hyperelastic Constitutive Parameters

Based on the results of the uniaxial tension, transverse compression, bias-extension, and out-of-plane shear tests, the macroscopic load–displacement data were converted into strain energy densities associated with different deformation modes through geometric normalization and energy-equivalence formulations. The relationships between the strain energy densities and the corresponding physical invariants were then obtained. To balance the capability of the constitutive model to describe nonlinear mechanical responses and the numerical stability of finite element calculations, polynomial functions were adopted to fit the energy responses. The specific forms of the strain energy density functions are defined as follows:

$$\psi_{\text{elong}}(I_{\text{elong}\alpha}) = \sum_{i=1}^{5} A_{\alpha i}(I_{\text{elong}\alpha})^i \quad (\alpha = 1, 2) \tag{14}$$

$$\psi_{\text{comp}}^{\text{thick}}(I_{\text{comp}}) = \sum_{i=1}^{3} B_i (I_{\text{comp}})^{2i} \tag{15}$$

$$\psi_{\text{shear}}^{\text{in-plane}}(I_{\text{cp}}) = \sum_{i=1}^{3} C_i (I_{\text{cp}})^{i} \tag{16}$$

$$\psi_{\text{shear}}^{\text{out-plane}}(I_{\text{ct}\alpha}) = \sum_{i=1}^{3} D_{\alpha i} (I_{\text{ct}\alpha})^{i} \quad (\alpha = 1, 2) \tag{17}$$

where $A_{\alpha i}$, B_i, C_i and $D_{\alpha i}$ are the material fitting parameters to be identified for the corresponding deformation modes.

The truncation orders of the polynomial strain energy density functions were determined according to the mechanical response characteristics of each deformation mode. The tensile response exhibits pronounced nonlinear stiffening in the large-deformation stage; therefore, a fifth-order polynomial was adopted to improve the fitting capability for the later-stage mechanical response. The transverse compression response was described using an even-order polynomial to ensure the continuity and numerical stability of the compression strain energy within the investigated compression range. By contrast, the nonlinearities of the in-plane and out-of-plane shear responses are relatively weak, and low-order polynomial functions are sufficient to characterize these responses.

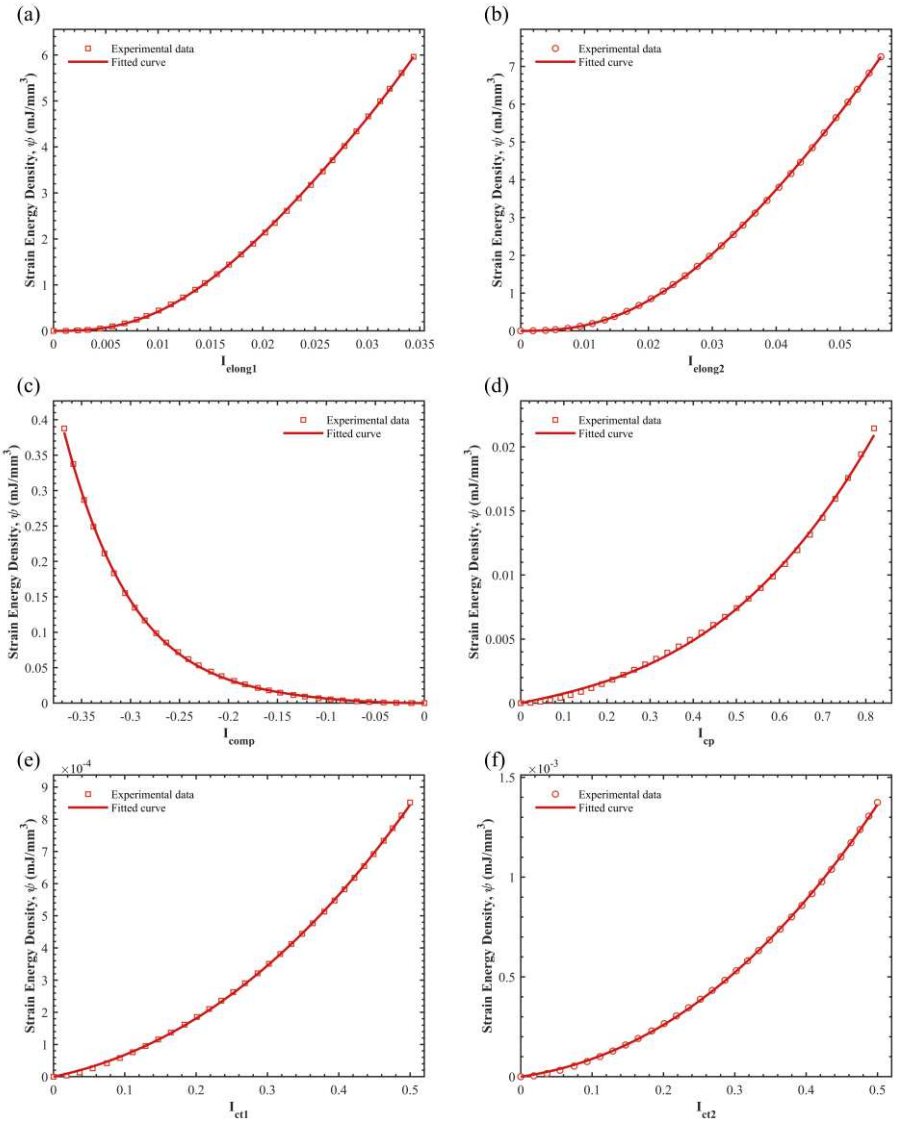


Fig. 6 Fitting results of the strain energy density functions with respect to the physical invariants under different decoupled deformation modes: (a) warp-direction tension; (b) weft-direction tension; (c) transverse compression; (d) in-plane shear; (e) warp-direction out-of-plane shear; (f) weft-direction out-of-plane shear

Fig. 6 shows the fitting results of the strain energy density functions for different deformation modes. The fitted curves agree well with the experimental data and effectively capture the nonlinear response characteristics of the corresponding deformation modes. Based on these fitting results, the identified material parameters are summarized in Table 3 and used as input parameters for the subsequent ABAQUS/VUMAT finite element implementation and forming simulations.

Table 3 Parameter matrix of the hyperelastic constitutive model for the three-dimensional angle-interlock preform

Deformation mode	Coefficient symbol	$i=1$	$i=2$	$i=3$	$i=4$	$i=5$
Warp tension	A_{1i}	0	6.25×10^{2}	5.25×10^{5}	-1.89×10^{7}	2.14×10^{8}
Weft tension	A_{2i}	0	5.96×10^{2}	1.11×10^{5}	-2.26×10^{6}	1.46×10^{7}
Transverse compression	B_i	6.28×10^{-1}	0	1.29×10^{1}	—	—
In-plane shear	C_i	6.85×10^{-3}	4.52×10^{-3}	2.23×10^{-2}	—	—
Warp-direction out-of-plane shear	D_{1i}	4.64×10^{-4}	2.04×10^{-3}	8.09×10^{-4}	—	—
Weft-direction out-of-plane shear	D_{2i}	5.18×10^{-4}	3.56×10^{-3}	1.72×10^{-3}	—	—

4 Model Validation and Forming Mechanism Analysis of the Three-Dimensional Angle-Interlock Preform

4.1 Hemispherical Forming Experiment and Deformation Characteristics

To validate the predictive capability of the established hyperelastic constitutive model for the forming behavior of the three-dimensional angle-interlock preform over complex surfaces, hemispherical forming was adopted as the validation benchmark in this study [45–51]. A square specimen with dimensions of 300 mm × 300 mm was used, and a white grid pattern was marked on the specimen surface to facilitate the measurement of the in-plane shear angle distribution after forming. As shown in Fig. 7(a), the specimen was clamped between two transparent blank-holder plates with a central opening radius of 60 mm. The bolt pre-tightening torque was controlled at 0.5 N·m to provide a uniform blank-holding constraint. A hemispherical punch with a radius of 50 mm was quasi-statically driven to a displacement of 50 mm at a loading rate of 20 mm/min. The displacement-controlled forming test was performed using a Shimadzu testing machine (AG-250kNE).

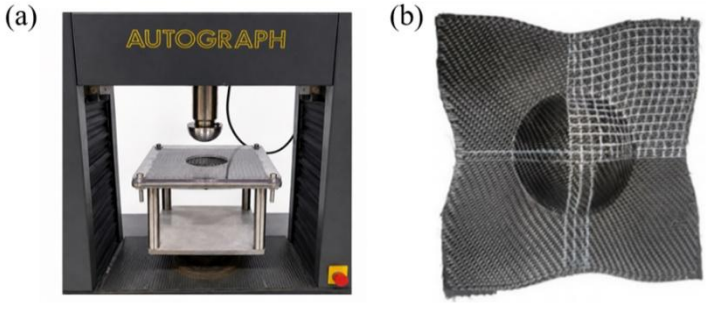


Fig. 7 Hemispherical forming experiment and formed configuration: (a) experimental setup; (b) formed configuration after hemispherical forming

Fig. 7(b) shows the formed configuration after hemispherical forming. During punch forming, the preform deforms from its initial planar state into a hemispherical configuration with an evident double-curvature feature. Owing to directional differences in warp/weft tensile stiffness, spatial yarn paths, and in-plane shear deformability, the formed boundary does not exhibit uniform inward draw-in, but shows

direction-dependent edge draw-in. The punch-contact region conforms to the hemispherical punch surface through overall bending, whereas the flange region remains approximately planar. The transition region between these two regions is simultaneously affected by curvature variation, blank-holding constraints, and yarn orientation, leading to more pronounced localized bending and yarn reorientation. Therefore, this transition region is further examined in the subsequent analyses of shear deformation and cross-sectional deformation.

Based on these experimental observations, the predictive capability of the established constitutive model is further evaluated by comparing the finite element results with the experimental data in terms of the macroscopic load response, in-plane shear angle distribution, boundary draw-in, and out-of-plane shear characteristics.

4.2 Validation of Hemispherical Forming Response and Analysis of Deformation Mechanism

A finite element model corresponding to the hemispherical forming experiment was developed in ABAQUS, as shown in Fig. 8. Considering the symmetry of the specimen geometry and boundary conditions, a quarter-symmetric model was adopted to improve computational efficiency. The geometries of the die and punch were defined according to the experimental setup. The preform was discretized using C3D8R solid elements. The contact friction coefficient between the specimen and the punch/blank-holder plates was set to 0.2. The established hyperelastic constitutive model was implemented in the finite element analysis through an ABAQUS/VUMAT user material subroutine.

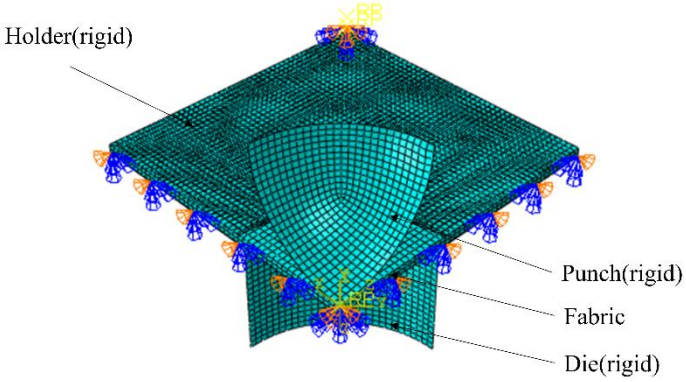


Fig. 8 Finite element model for hemispherical forming

4.2.1 Macroscopic Load Response and Stiffness Evolution

Fig. 9 compares the experimental and simulated load–displacement curves during hemispherical forming. The two curves exhibit similar nonlinear increasing responses and show good overall agreement, with a relative error of approximately 15.2% in the peak load. In the initial stage of punch displacement, the preform mainly undergoes localized bending and initial conformity with the punch surface in the punch-contact region, whereas in-plane shear and boundary draw-in are not yet significant. Therefore, the load increases slowly. As the punch displacement increases, in-plane shear in the curvature transition region gradually intensifies, and the edge draw-in is restricted by blank-holding friction. Consequently, the overall forming resistance increases, as reflected by the increased slope of the load–displacement curve. The simulated load is slightly higher than the experimental value in the middle and later stages, which is mainly attributed to the use of a constant friction coefficient in the finite element model. This treatment does not fully account for the dynamic variation in contact pressure between the preform and the forming tools during the actual forming process.

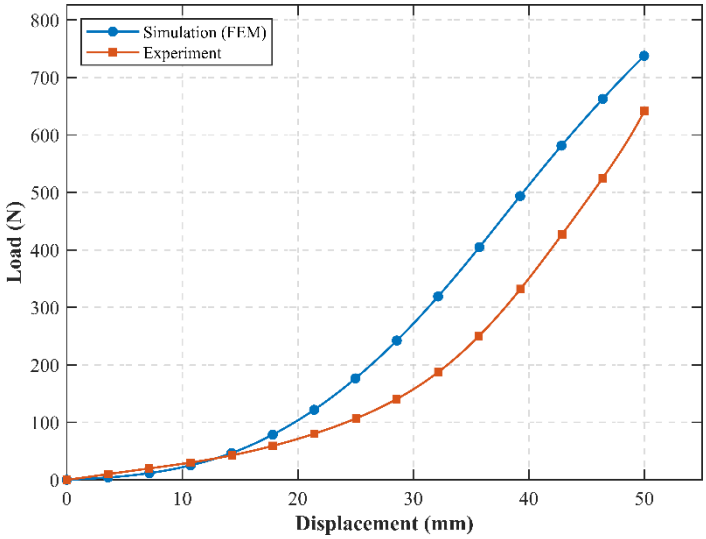


Fig. 9 Comparison between experimental and simulated macroscopic load–displacement responses of the preform during hemispherical forming

4.2.2 In-Plane Shear Angle Distribution and Pathwise Validation

Fig. 10 shows the finite element distributions of the in-plane shear angle of the preform after hemispherical forming. Fig. 10(a) presents the shear angle distribution in the overall deformed configuration, whereas Fig. 10(b) and (c) show the shear angle contours from the convex and concave sides, respectively. Compared with the experimental formed configuration shown in Fig. 7(b), the simulated results reasonably reproduce the overall conformation of the preform to the hemispherical punch surface, and the hemispherical punch-contact region, flange region, and curvature transition region are all well represented.

The in-plane shear angle exhibits an approximately centrosymmetric distribution. Regions with elevated in-plane shear angles are mainly concentrated in the curvature transition region and extend along the 45° bias directions. The high-shear regions on the convex side in Fig. 10(b) correspond to the regions where pronounced deformation of the surface grid is observed in the experiment. Fig. 10(c) further shows that the in-plane shear concentration in the transition region on the concave side is more pronounced than that on the convex side, with a maximum in-plane shear angle of approximately 37.4°.

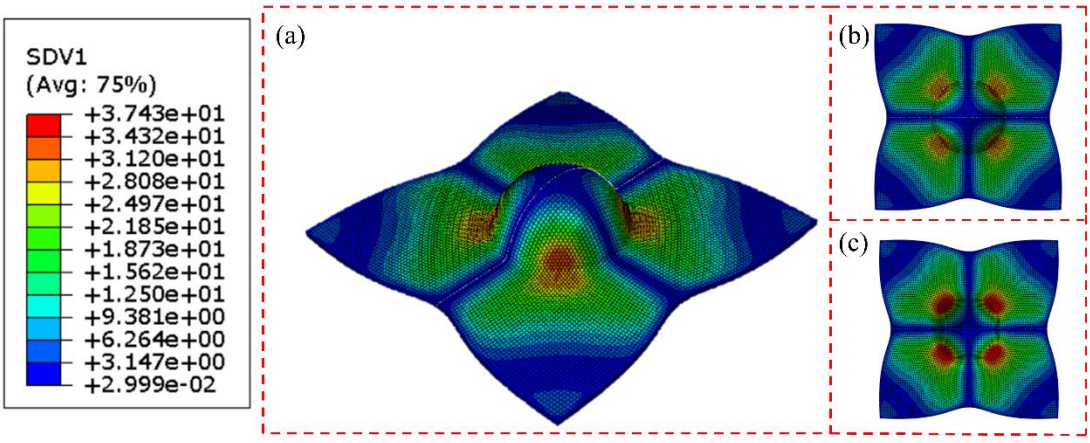


Fig. 10 In-plane shear angle distribution after hemispherical forming: (a) overall view; (b) convex-side view; (c) concave-side view

To quantitatively evaluate the predictive capability of the model for in-plane shear deformation, the

45° diagonal direction on the convex side was selected as the shear angle extraction path, as shown in Fig. 11. The finite element predictions are generally consistent with the experimental measurements in terms of the overall variation trend. Along the 45° path on the convex side from the forming center toward the boundary, the shear angle first increases gradually and reaches a peak at approximately 70–95 mm from the center, with a predicted peak value of approximately 34° and an experimentally measured peak value of approximately 32°. The shear angle then decreases continuously and approaches zero near the boundary, showing an overall single-peak distribution. The peak region corresponds to the curvature transition region. Under the combined effects of curvature variation and blank-holder constraint, relative rotation between warp and weft yarns occurs to accommodate the deformation of the planar preform into a double-curvature surface; therefore, shear deformation is more pronounced in this region. By contrast, the edge region is constrained by the blank holder and contact friction, which restricts in-plane deformation and results in a relatively small shear angle. These results indicate that the model can reasonably predict the evolution of the shear angle along the 45° path on the convex side.

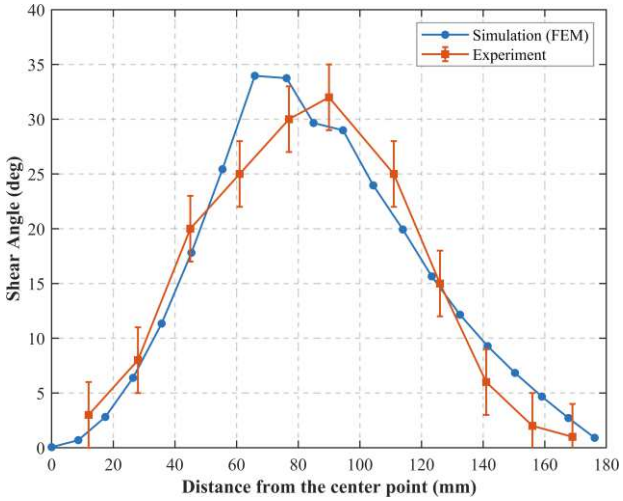


Fig. 11 Comparison between simulated and experimental shear angle distributions along the 45° direction of the preform

4.2.3 Boundary Draw-in and Contour Evolution

Fig. 12 compares the experimentally measured and numerically predicted boundary contours of the preform after hemispherical forming. The dashed line denotes the initial specimen boundary, while the solid line and discrete markers represent the simulated and experimental final contours, respectively. The formed boundary exhibits clear directional dependence rather than uniform radial draw-in. More pronounced edge draw-in occurs along the warp and weft directions, which can be attributed to the relatively high axial tensile stiffness of the yarns in these directions. As yarn elongation is limited during forming, the preform mainly accommodates the double-curvature deformation through in-plane displacement of the edge region. By contrast, deformation along the 45° bias direction is more readily accommodated by in-plane shear arising from the relative rotation between warp and weft yarns, resulting in a smaller boundary shift in this direction. Overall, the simulated contour agrees well with the experimental measurement, indicating that the proposed model can reasonably capture the boundary evolution of the preform during hemispherical forming. The remaining local discrepancies may be related to the simplified friction treatment, local yarn slippage, and nonuniform blank-holding constraints in the experiment.

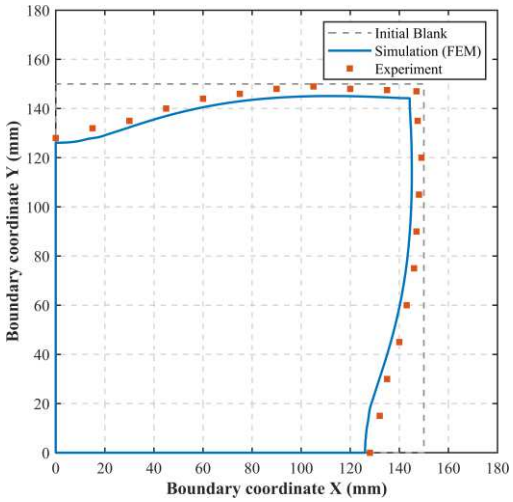


Fig. 12 Comparison between experimentally measured and numerically predicted boundary draw-in contours after hemispherical forming

4.2.4 Characteristics of Out-of-Plane Shear Deformation

To characterize the out-of-plane shear deformation behavior of the preform during hemispherical forming, Fig. 13 presents the experimental cross-sectional profiles and the finite element distributions of the out-of-plane shear angle on the x–z and y–z sections. In the finite element results, the out-of-plane shear angle is derived from the physical invariants defined in Eq. (8) and used to quantitatively describe the relative through-thickness deflection at a material point and its deviation from the initial orthogonal state. The contours show that the out-of-plane shear angle distributions on the two sections are generally consistent. Regions with relatively high out-of-plane shear angles are mainly concentrated in the curvature transition region, whereas the out-of-plane shear angles in the flange region and the hemispherical punch-contact region remain relatively low. The maximum out-of-plane shear angles on the x–z and y–z sections are approximately 17.47° and 17.52°, respectively, indicating only a slight difference between the two peak values. In the experimental cross-sectional profiles, the transition region also exhibits more pronounced localized bending and through-thickness yarn deflection, which generally coincides with the out-of-plane shear concentration regions predicted by the finite element contours.

Fig. 14 further shows the local yarn deflection in the transition regions of the experimental sections. The local yarn bundle deflection angle ranges from approximately 10° to 21° in the x–z section and from 11° to 23° in the y–z section. Both sections exhibit evident through-thickness yarn deflection in the transition region, which is consistent with the finite element prediction of out-of-plane shear concentration in this region. Therefore, during hemispherical forming, the transition region undergoes not only overall bending but also relative interlayer deflection and through-thickness shear deformation, serving as the main region where the preform accommodates local curvature variation. As an important three-dimensional deformation mechanism in the complex-surface forming of three-dimensional woven preforms, out-of-plane shear deformation enables the preform to accommodate local curvature variation through relative through-thickness yarn deflection, thereby enhancing its conformation to the tool surface.

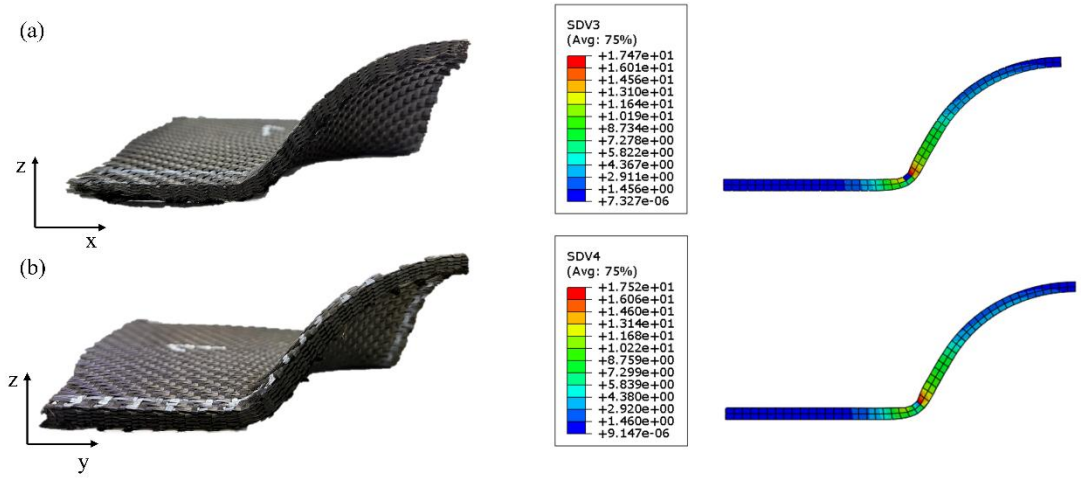


Fig. 13 Experimental and simulated comparison of the out-of-plane shear angle during hemispherical forming: (a) out-of-plane shear angle γ_{48} on the x–z section; (b) out-of-plane shear angle γ_{68} on the y–z section

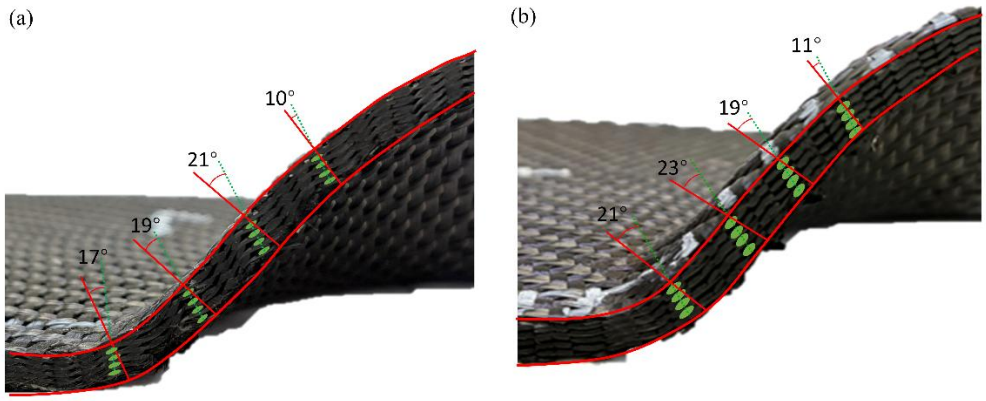


Fig. 14 Yarn deflection angles in the sectional transition region: (a) x–z section; (b) y–z section

4.3 Effect of Initial Yarn Orientation on Forming Behavior

The three-dimensional angle-interlock preform exhibits pronounced orthotropic characteristics, and its forming behavior is jointly affected by the initial warp/weft yarn orientation, the geometric constraints imposed by the forming tools, and boundary friction conditions. Changing the initial yarn orientation modifies the relative alignment between the warp/weft yarn directions and the principal geometric axes of the forming tools, thereby affecting the spatial distribution of in-plane shear deformation and the overall forming pattern. To analyze the effect of initial yarn orientation on forming behavior, finite element models with [±45°] and asymmetric [30°/−60°] yarn orientations were further developed for comparison, while the tool dimensions, material parameters, and boundary conditions were kept unchanged. The [0°/90°] orientation was used as the reference case. For the [30°/−60°] orientation, the warp and weft yarn directions are no longer symmetric with respect to the geometric symmetry axes of the model. Therefore, a full model was adopted to avoid the influence of symmetry boundary conditions on the evolution of the boundary contour and the distribution of the shear field.

The preceding hemispherical forming validation shows that, under the [0°/90°] orientation, the shear angle field exhibits an approximately centrosymmetric distribution, with regions of relatively high shear angles mainly located in the curvature transition region. On this basis, the changes in the in-plane shear angle distribution and formed contour induced by different initial yarn orientations were further analyzed.

As shown in Fig. 15(a), when the yarn orientation is changed to [±45°], the warp and weft yarn directions are rotated by 45° relative to the principal axes of the forming tools, leading to a corresponding redistribution of the shear field. Compared with the [0°/90°] orientation, the high-shear regions are no longer mainly located along the diagonal directions of the curvature transition region, but shift to symmetric regions distributed along the principal axes of the forming tools. This result indicates that the initial yarn orientation primarily affects the spatial distribution of the high-shear regions, while exerting a relatively limited influence on the magnitude of the maximum shear angle.

For the asymmetric [30°/−60°] orientation, the shear angle distribution shown in Fig. 15(b) no longer exhibits an evident centrosymmetric pattern but instead presents pronounced nonuniformity and directional bias. The high-shear regions undergo a distinct spatial shift, and the formed contour also exhibits a certain degree of twisting. This indicates that an asymmetric yarn orientation changes the alignment between material anisotropy and the geometric constraints imposed by the forming tools, so that the differences between the warp and weft directions are no longer distributed in a centrosymmetric manner. Consequently, the shear field is redistributed, and deflection of the boundary contour is induced.

In summary, the initial yarn orientation significantly affects the evolution of the shear field during hemispherical forming of the three-dimensional woven preform. This influence is reflected primarily not by a substantial change in the maximum shear angle, but by the spatial redistribution of high-shear regions, local deformation patterns, and boundary contour evolution. Therefore, optimization of the yarn orientation can be used to regulate local deformation concentration, providing a basis for process design and forming-quality improvement of three-dimensional woven preforms.

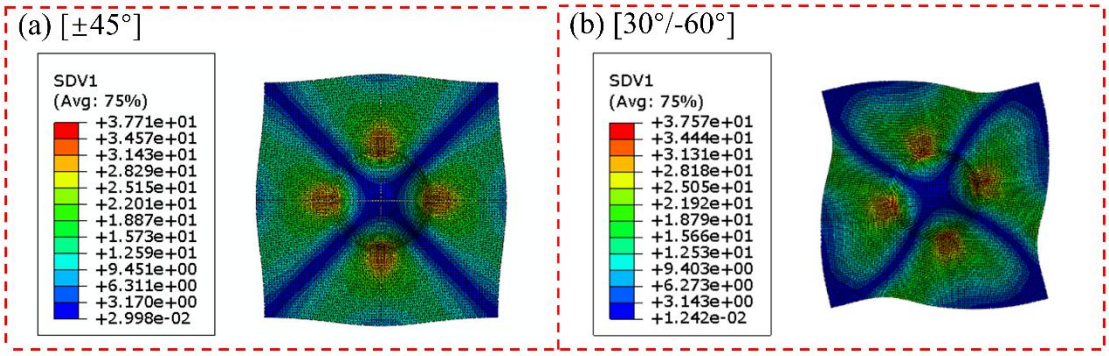


Fig. 15 In-plane shear angle distributions under different initial yarn orientations during hemispherical forming: (a) [±45°]; (b) [30°/−60°]

5 Conclusions

In this study, a 1/3 twill three-dimensional angle-interlock carbon fiber preform was investigated, and a multi-mode decoupled hyperelastic constitutive model was established to describe its large-deformation and anisotropic mechanical responses during forming over complex surfaces. The strain energy density responses and material parameters associated with different deformation modes were identified through mechanical characterization tests, and the model was implemented in ABAQUS/Explicit via a VUMAT user material subroutine. Comparative validation with hemispherical forming experiments shows that the established model can reasonably predict the macroscopic load response, boundary draw-in behavior, and local shear deformation characteristics of the preform. The forming mechanism analysis indicates that in-plane shear is the dominant deformation mode by which the preform accommodates a double-curvature surface, whereas out-of-plane shear improves local surface conformity in the curvature transition region through local through-thickness yarn deflection. Further analysis of the forming behavior under different initial yarn orientations shows that the initial

yarn orientation mainly changes the spatial distribution of high-shear regions, while exerting limited influence on the magnitude of the maximum shear angle. These results provide a reference for complex-surface forming simulation, yarn orientation design, and regulation of local deformation concentration in three-dimensional woven preforms.

Since a multi-mode decoupled constitutive description was adopted in this study, the coupling effects among different deformation modes were not fully considered. Future work will focus on developing a coupled constitutive model that accounts for the interactions among tension, compression, in-plane shear, and out-of-plane shear, so as to more accurately characterize the nonlinear mechanical response of the material during complex-surface forming.

Author contributions Zhenyu Wang: Methodology, Investigation, Data curation, Formal analysis, Writing - original draft. **Yifan Zhang**: Conceptualization, Funding acquisition, Writing - review & editing. **Jiahui Wei**: Investigation, Formal analysis. **Qiwei Guo** and **Daijun Zhang**: Software, Visualization. **Chao Li** and **Junjie Hao**: Resources, Project administration. **Pengfei Jiang** and **Tianqi Wang**: Visualization, Data curation. **Li Chen**: Validation, Supervision.

Acknowledgements This work was supported by the National key research and development program of China (No. 2023YFB3709800), National science and Technology Major Project, China (No. 2025ZD0613400), National Science and Technology Project (No. 50922020401).

Data availability The data that support the findings of this study are available from the corresponding author upon reasonable request.

Declarations

Competing Interests The authors declare no competing interests.

References

[1] Mouritz, A.P., Bannister, M.K., Falzon, P.J., Leong, K.H.: Review of applications for advanced three-dimensional fibre textile composites. Compos. Part A Appl. Sci. Manuf. 30(12), 1445–1461 (1999). https://doi.org/10.1016/S1359-835X(99)00034-2

[2] Gries, T., Bettermann, I., Blaurock, C., et al.: Aachen technology overview of 3D textile materials and recent innovation and applications. Appl. Compos. Mater. 29(1), 43–64 (2022). https://doi.org/10.1007/s10443-022-10011-w

[3] Dang, M.-G., Li, D.-S., Jiang, L.: Temperature effects on mechanical response and failure mechanism of 3D angle-interlock woven carbon/epoxy composites. Compos. Commun. 18, 37–42 (2020). https://doi.org/10.1016/j.coco.2020.01.001

[4] Li, D.-S., Dang, M.-G., Jiang, L.: Fatigue behavior and failure mechanisms of 3D angle-interlock woven composite at room and cryogenic temperatures under bending. Compos. Commun. 23, 100559 (2021). https://doi.org/10.1016/j.coco.2020.100559

[5] Han, C., Liu, J., Li, Z., Yao, Y., Su, Y.: Anisotropy characteristics of electrical conductivity and compressive strength of 3D carbon fiber/epoxy angle-interlock woven composites. Compos. Commun. 47, 101879 (2024). https://doi.org/10.1016/j.coco.2024.101879

[6] Guo, Q., Zhang, Y., Li, D., Sun, X., Li, M., Chen, L.: Experimental characterization of the compressive properties and failure mechanism of novel multiaxial 3D woven composites. Compos. Commun. 28, 100905 (2021). https://doi.org/10.1016/j.coco.2021.100905

[7] Bandaru, A.K., Sachan, Y., Ahmad, S., Alagirusamy, R., Bhatnagar, N.: On the mechanical response of 2D plain woven and 3D angle-interlock fabrics. Compos. Part B Eng. 118, 135–148 (2017). https://doi.org/10.1016/j.compositesb.2017.03.011

[8] Gereke, T., Döbrich, O., Hübner, M., Cherif, C.: Experimental and computational composite textile reinforcement forming: A review. Compos. Part A Appl. Sci. Manuf. 46, 1–10 (2013). https://doi.org/10.1016/j.compositesa.2012.10.004

[9] Zhang, Y., You, M., Guo, Q., Li, C., Zhang, D., Shi, D., Zhang, J., Sun, Z., Zhang, P., Wang, T., Chen, L.: A review of the formability of woven fabrics for composite materials. Polym. Compos. 45(16), 14498–14520 (2024). https://doi.org/10.1002/pc.28837

[10] Yang, T., Zhang, L., Li, Z., Huang, K., Guo, L.: Experimental characterization methods and numerical models of woven composite preforms: A review. Compos. Part A Appl. Sci. Manuf. 185, 108329 (2024). https://doi.org/10.1016/j.compositesa.2024.108329

[11] Chowdhury, I.R., Summerscales, J.: Woven fabrics for composite reinforcement: A review. J. Compos. Sci. 8(7), 280 (2024). https://doi.org/10.3390/jcs8070280

[12] Wang, H., Wang, Z., Wang, B., Fang, G., Meng, S.: Kinematic modeling with Micro-CT slice auxiliary calibration for 2.5D woven SiO2f/SiO2 composites. Compos. Commun. 40, 101613 (2023). https://doi.org/10.1016/j.coco.2023.101613

[13] Zhao, Z., Wei, H., Cai, Y., Lv, Q., Zhou, J., Zhang, C.: Predicting the low-velocity impact failure of 3D woven composites based on a local homogenization modeling strategy. Compos. Commun. 48, 101912 (2024). https://doi.org/10.1016/j.coco.2024.101912

[14] Van der Weeën, F.: Algorithms for draping fabrics on doubly-curved surfaces. Int. J. Numer. Methods Eng. 31(7), 1415–1426 (1991). https://doi.org/10.1002/nme.1620310712

[15] Dong, L., Lekakou, C., Bader, M.G.: Solid-mechanics finite element simulations of the draping of fabrics: a sensitivity analysis. Compos. Part A Appl. Sci. Manuf. 31(7), 639–652 (2000). https://doi.org/10.1016/S1359-835X(00)00046-4

[16] Colin, D., Bel, S., Hans, T., Hartmann, M., Drechsler, K.: Virtual description of non-crimp fabrics at the scale of filaments including orientation variability in the fibrous layers. Appl. Compos. Mater. 27(4), 337–355 (2020). https://doi.org/10.1007/s10443-020-09819-1

[17] Boisse, P., Zouari, B., Daniel, J.-L.: Importance of in-plane shear rigidity in finite element analyses of woven fabric composite preforming. Compos. Part A Appl. Sci. Manuf. 37(12), 2201–2212 (2006). https://doi.org/10.1016/j.compositesa.2005.09.018

[18] Wei, Q., Zhang, D.: A textile architecture-based discrete modeling approach to simulating fabric draping processes. J. Ind. Text. 53, 15280837231159678 (2023). https://doi.org/10.1177/15280837231159678

[19] Chen, Z., Wang, B., Pan, S., Fang, G., Meng, S., Zhou, Z., Zhu, J.: Damage analysis of shear pre-deformed 3D angle-interlock woven composites using experiment and non-orthogonal finite element model. Compos. Commun. 28, 100978 (2021). https://doi.org/10.1016/j.coco.2021.100978

[20] Peng, X.Q., Cao, J.: A continuum mechanics-based non-orthogonal constitutive model for woven composite fabrics. Compos. Part A Appl. Sci. Manuf. 36(6), 859–874 (2005). https://doi.org/10.1016/j.compositesa.2004.08.008

[21] Sun, D., Zhang, W., Zou, J., Xiong, Y., Tang, C., Zhang, W.: Coupled 3D non-orthogonal constitutive model for woven composites in preforming and compaction processes. Manuf. Lett. 41, 412–420 (2024). https://doi.org/10.1016/j.mfglet.2024.09.049

[22] Khan, M.A., Mabrouki, T., Vidal-Sallé, E., Boisse, P.: Numerical and experimental analyses of woven composite reinforcement forming using a hypoelastic behaviour. Application to the double dome benchmark. J. Mater. Process. Technol. 210(2), 378–388 (2010). https://doi.org/10.1016/j.jmatprotec.2009.09.027

[23] Aimene, Y., Hagege, B., Sidoroff, F., Vidal-Sallé, E., Boisse, P., Dridi, S.: Hyperelastic approach for composite reinforcement forming simulations. Int. J. Mater. Form. 1(S1), 811–814 (2008). https://doi.org/10.1007/s12289-008-0259-x

[24] Aimène, Y., Vidal-Sallé, E., Hagège, B., Sidoroff, F., Boisse, P.: A hyperelastic approach for composite reinforcement large deformation analysis. J. Compos. Mater. 44(1), 5–26 (2010). https://doi.org/10.1177/0021998309345348

[25] Peng, X., Guo, Z., Du, T., Yu, W.-R.: A simple anisotropic hyperelastic constitutive model for textile fabrics with application to forming simulation. Compos. Part B Eng. 52, 275–281 (2013). https://doi.org/10.1016/j.compositesb.2013.04.014

[26] Yin, H., Peng, X., Du, T., Guo, Z.: Draping of plain woven carbon fabrics over a double-curvature mold. Compos. Sci. Technol. 92, 64–69 (2014). https://doi.org/10.1016/j.compscitech.2013.12.013

[27] Charmetant, A., Orliac, J.G., Vidal-Sallé, E., Boisse, P.: Hyperelastic model for large deformation analyses of 3D interlock composite preforms. Compos. Sci. Technol. 72(12), 1352–1360 (2012). https://doi.org/10.1016/j.compscitech.2012.05.006

[28] Zhang, X., Zhang, S., Zhang, H., Liu, C., Zhou, Y., Dong, C., Gao, X., Wang, F., Song, Y.: A hyperelastic model considering the coupling of shear-compression for the forming simulation of 3D orthogonal composite preforms. Compos. Sci. Technol. 258, 110884 (2024). https://doi.org/10.1016/j.compscitech.2024.110884

[29] Liu, C., Huang, T., Di, J., Cheng, H., Liang, B.: An anisotropic hyperelastic constitutive model for predicting preforming deformation of 3D woven fabrics. Aeronaut. Sci. Technol. 35(3), 28–40 (2024). https://doi.org/10.19452/j.issn1007-5453.2024.03.004

[30] Yousaf, Z., Potluri, P., Withers, P.J.: Influence of tow architecture on compaction and nesting in textile preforms. Appl. Compos. Mater. 24(2), 337–350 (2017). https://doi.org/10.1007/s10443-016-9554-8

[31] Wu, W., Jiang, B., Xie, L., Klunker, F., Aranda, S., Ziegmann, G.: Effect of compaction and preforming parameters on the compaction behavior of bindered textile preforms for automated composite manufacturing. Appl. Compos. Mater. 20(5), 907–926 (2013). https://doi.org/10.1007/s10443-012-9308-1

[32] He, Y., Mei, M., Wei, K., Duan, S., Yang, X., Han, X.: Modelling the viscoelastic compaction behavior of 3D stitched carbon fabric with different stitching parameters. Compos. Commun. 21, 100410 (2020). https://doi.org/10.1016/j.coco.2020.100410

[33] Mahadik, Y., Robson Brown, K.A., Hallett, S.R.: Characterisation of 3D woven composite internal architecture and effect of compaction. Compos. Part A Appl. Sci. Manuf. 41(7), 872–880 (2010). https://doi.org/10.1016/j.compositesa.2010.02.019

[34] Cao, J., Akkerman, R., Boisse, P., et al.: Characterization of mechanical behavior of woven fabrics: Experimental methods and benchmark results. Compos. Part A Appl. Sci. Manuf. 39(6), 1037–1053 (2008). https://doi.org/10.1016/j.compositesa.2008.02.016

[35] Boisse, P., Hamila, N., Guzman-Maldonado, E., Madeo, A., Hivet, G., dell'Isola, F.: The bias-extension test for the analysis of in-plane shear properties of textile composite reinforcements and prepregs: a review. Int. J. Mater. Form. 10(4), 473–492 (2017). https://doi.org/10.1007/s12289-016-1294-7

[36] Harrison, P., Clifford, M.J., Long, A.C.: Shear characterisation of viscous woven textile composites: a comparison between picture frame and bias extension experiments. Compos. Sci. Technol. 64(10–11), 1453–1465 (2004). https://doi.org/10.1016/j.compscitech.2003.10.015

[37] Mohammed, U., Lekakou, C., Dong, L., Bader, M.G.: Shear deformation and micromechanics of woven fabrics. Compos. Part A Appl. Sci. Manuf. 31(4), 299–308 (2000). https://doi.org/10.1016/S1359-835X(99)00081-0

[38] Bel, S., Boisse, P., Dumont, F.: Analyses of the deformation mechanisms of non-crimp fabric composite reinforcements during preforming. Appl. Compos. Mater. 19(3–4), 513–528 (2012). https://doi.org/10.1007/s10443-011-9207-x

[39] Stamati, O., Orgéas, L., Rolland du Roscoat, S., Lhuissier, P., Dumont, P.J.J., Martoïa, F.: Advanced analysis of the bias-extension of woven fabrics with X-ray microtomography and Digital Volume Correlation. Compos. Part A Appl. Sci. Manuf. 175, 107748 (2023). https://doi.org/10.1016/j.compositesa.2023.107748

[40] Mei, M., Huang, J., Yu, S., Zeng, T., He, Y., Wei, K.: Shear deformation characterization and normalized method of tricot-stitched unidirectional non-crimp fabric. Compos. Sci. Technol. 246, 110391 (2024). https://doi.org/10.1016/j.compscitech.2023.110391

[41] Launay, J., Hivet, G., Duong, A.V., Boisse, P.: Experimental analysis of the influence of tensions on in plane shear behaviour of woven composite reinforcements. Compos. Sci. Technol. 68(2), 506–515 (2008). https://doi.org/10.1016/j.compscitech.2007.06.021

[42] Komeili, M., Milani, A.S.: On effect of shear-tension coupling in forming simulation of woven fabric reinforcements. Compos. Part B Eng. 99, 17–29 (2016). https://doi.org/10.1016/j.compositesb.2016.05.004

[43] Harrison, P., Fernandez Alvarez, M., Anderson, D.: Towards comprehensive characterisation and modelling of the forming and wrinkling mechanics of engineering fabrics. Int. J. Solids Struct. 154, 2–18 (2018). https://doi.org/10.1016/j.ijsolstr.2016.11.008

[44] Moezzi, M., Haji-Badali, A., Barez, F.: Analysis of the wrinkle geometry of the woven fabrics during uniaxial bias extension test using Ricker wavelet algorithm. Compos. Part A Appl. Sci. Manuf. 141, 106230 (2021). https://doi.org/10.1016/j.compositesa.2020.106230

[45] De Luycker, E., Morestin, F., Boisse, P., Marsal, D.: Simulation of 3D interlock composite preforming. Compos. Struct. 88(4), 615–623 (2009). https://doi.org/10.1016/j.compstruct.2008.06.005

[46] Hamila, N., Boisse, P.: A meso-macro three node finite element for draping of textile composite preforms. Appl. Compos. Mater. 14(4), 235–250 (2007). https://doi.org/10.1007/s10443-007-9043-1

[47] Dufour, C., Wang, P., Boussu, F., Soulat, D.: Experimental investigation about stamping behaviour of 3D warp interlock composite preforms. Appl. Compos. Mater. 21(5), 725–738 (2014). https://doi.org/10.1007/s10443-013-9369-9

[48] Liu, M., Wang, L., Peng, X.: Testing, characterizing, and forming of glass twill fabric/polypropylene prepregs. J. Compos. Mater. 53(28–30), 3939–3950 (2019). https://doi.org/10.1177/0021998319851215

[49] Jiao, W., Chen, L., Xie, J., Yang, Z., Guo, Z.: Deformation mechanisms of 3D LTL woven preforms in hemisphere forming tests. Compos. Struct. 283, 115156 (2022). https://doi.org/10.1016/j.compstruct.2021.115156

[50] Vanclooster, K., Lomov, S.V., Verpoest, I.: Experimental validation of forming simulations of fabric reinforced polymers using an unsymmetrical mould configuration. Compos. Part A Appl. Sci. Manuf. 40(4), 530–539 (2009). https://doi.org/10.1016/j.compositesa.2009.02.005

[51] Wu, Z., Lu, T., Shi, L., Li, H., Cheng, X., Camilleri, D.: The effect of blank holder gap on yarn local buckling during forming of woven CFRP preform with complex geometries. Appl. Compos. Mater. 32(6), 2769–2787 (2025). https://doi.org/10.1007/s10443-025-10369-7